Provided for non-commercial research and education use.
Not for reproduction, distribution or commercial use.


This article appeared in a journal published by Elsevier. The attached copy is furnished to the author for internal non-commercial research and education use, including for instruction at the authors institution and sharing with colleagues.

Other uses, including reproduction and distribution, or selling or licensing copies, or posting to personal, institutional or third party websites are prohibited.

In most cases authors are permitted to post their version of the article (e.g. in Word or Tex form) to their personal website or institutional repository. Authors requiring further information regarding Elsevier's archiving and manuscript policies are encouraged to visit:

http://www.elsevier.com/authorsrights

Author's personal copy

International Journal of Heat and Mass Transfer 64 (2013) 514–525

Contents lists available at SciVerse ScienceDirect

International Journal of Heat and Mass Transfer

journal homepage: www.elsevier.com/locate/ijhmt

# On a transitional and turbulent natural convection in spherical shells

Yuri Feldman *, Tim Colonius

*California Institute of Technology, Pasadena, CA 91125, United States*

ARTICLE INFO

*Article history:*
Received 3 December 2012
Received in revised form 15 April 2013
Accepted 15 April 2013

*Keywords:*
Laminar and turbulent natural convection
Narrow spherical shells
*Nu–Ra* functional relation

ABSTRACT

Laminar and turbulent natural convection inside concentric spherical shells with isothermal cold and hot boundaries is numerically investigated up to Rayleigh number values $Ra \leqslant 10^{12}$ and $Pr = 0.71$. The study utilizes direct numerical simulation (DNS), large eddy simulation (LES) and Reynolds averaged Navier–Stokes (RANS) approaches for investigation of the laminar, transitional and fully developed turbulent flow regimes, respectively. Three-dimensional flow patterns for slightly supercritical oscillatory flow regime inside the shell, with internal/external diameter ratio equal to $D_i/D_o = 0.714$ are presented and may be potentially useful for verification of the future linear stability analysis results. Particular attention has been given to the complex, fully three-dimensional unsteady flows occurring in narrow shell geometries characterized by $0.85 \leqslant D_i/D_o \leqslant 0.95$. For this geometry considerable deviations in predicted heat flux rate through the shell boundaries are observed when compared with existing heat transfer correlations for the entire range of *Ra* numbers. The deviations tend to increase for transitional and fully turbulent flows. A new correlation for the heat transfer rate is suggested for laminar and transitional flow regimes.

© 2013 Elsevier Ltd. All rights reserved.

## 1. Introduction

Natural convection in confined geometries is of a great scientific and engineering interest. Depending on the heat source, the flow may be classified in three main groups: internal heat production, heating an enclosure from below (Rayleigh–Bénard configuration), heating an enclosure from its sides (e.g. differentially heated cavities). The second group has been used as a model problem for investigation of the transition process from steady flow to the fully developed turbulent regime through a rich sequence of bifurcations that enable the study of different transition mechanisms (see e.g. Clever and Busse [1], Busse [2], Gollub and Benson [3], Curry et al. [4], Daniels and Ong [5]). The first and the third groups are of importance in chemical and nuclear industries (see e.g. Gabor et al. [6]) as well in the manufacture of bulk semiconductor crystals Thevenard et al. [7].

Free convection flow inside spherical shells whose internal and external boundaries are held at constant hot and cold temperature, respectively is a stand alone and even more challenging configuration, since it locally resembles both Rayleigh–Bénard convection (at the top of the shell) and the differentially heated cavity (at the near-equatorial region), while its bottom region is almost thermally stable. Moreover, the instabilities and transition scenarios depend sensitively on the hot-cold configuration of the shell boundaries and on the internal to external diameter ratio $\phi = D_i/Do$. This ratio gives rise to different flow patterns starting from "modified kidney shaped eddy" for deep shells ($\phi \leqslant 0.5$) going to "interior expansion–contraction" for ($0.5 \leqslant \phi \leqslant 0.65$) then transforming into "three dimensional spiral" flow for ($0.65 \leqslant \phi \leqslant 0.85$) and finally ending up with "falling vortices" pattern for narrow shells ($0.85 \leqslant \phi$), as categorized by Powe et al.[8] for the shells with internal hot and external cold boundaries. At the same time "dripping blob" unsteady phenomenon was observed by Futterer et al. [9] inside the shells of large and moderate depths ($0.41 \leqslant \phi \leqslant 0.71$) with cold internal and hot external boundaries for $Pr = \infty$.

The analysis of narrow shells is a primary purpose of the present work. Their consideration is motivated by a recent study of Feldman et al. [10], where the performance of the scaled double-walled Titan Montgolfiere operating at cryogenic temperatures was investigated. Given Titan's low gravity (one-seventh of Earth) and cryogenic atmospheric temperatures (72*K*–94*K*), heated hot air balloon is an attractive configuration for a robotic vehicle for exploration of Titan, see e.g. Dorrington [11]. The double-walled Titan Montgolfiere was idealized by two massless rigid concentric spheres characterized by tending to zero values of surface thickness and thermal resistance, whereas the thin spherical shell plays the role of an insulating gap. The study presents an accurate analysis of free convection flow inside stationary fully inflated balloon and does not account for the possible variation of its shape (due to the balloon vibrations) and forced convection effects (showing up at possible balloon's rotation, deployment or ascend/descend phases). Despite the simplifications made, Feldman et al. [10]

* Corresponding author. Tel.: +1 6268636802.
*E-mail address:* feldy77@gmail.com (Y. Feldman).

0017-9310/$ - see front matter © 2013 Elsevier Ltd. All rights reserved.
http://dx.doi.org/10.1016/j.ijheatmasstransfer.2013.04.042

Author's personal copy



reported significant discrepancy between numerically and experimentally determined lift forces compared to those obtained by applying engineering correlations for the insulating gap.

In order to resolve these discrepancies, we perform simulations of laminar, transitional and fully turbulent flow regimes for three idealized narrow shells ($\phi = 0.85, 0.9, 0.95$) with isothermal surfaces. To provide the most favorable comparison possible with existing correlations uniform temperature of the balloon boundaries was assumed, which is plausible for the typical full scale Titan Montgolfiere ($D_o = 15m$) operating with $2kW$ heat source. In all simulations the value of $Pr$ number is set to $Pr = 0.71$, corresponding to nitrogen which is a primary component of the Titan's atmosphere (and very similar to air at standard pressure and temperature). The heat flux values obtained for laminar and transitional flows are then used to derive a new correlation based on a power law. Utilizing both DNS and LES approaches for simulation of fully developed turbulent flows inside the narrow shells is prohibitively expensive in terms of available CPU and time resources. Therefore the later is simulated by RANS with standard wall functions for modeling the turbulence and wall effects respectively.

The study also extends a numerical data of Scurtu et al. [12] by focussing on a slightly supercritical flow inside the shell with $\phi = 0.714$. In that case the flow is dominated by a single most energetic oscillating eigenvector whose absolute value is close to the spatial distribution of the oscillation amplitudes averaged over a number of periods, see e.g. Feldman and Gelfgat [13]. The reported spatial distribution of the oscillation amplitudes for each velocity component and temperature fields is an additional contribution of the present work and may be useful for verification of the future linear stability analysis results.

## 2. Computational details

Free convection flow inside a spherical shell with the internal hot and external cold boundaries is considered. The gravity $\mathbf{g}$ is constant and pointing along the negative $y$ axis $\mathbf{g} = -g\hat{y}$ as shown in Fig. 1(a). The problem is solved in Cartesian coordinates $(x,y,z)$ whose origin is located at the center of the shell. A pseudo-structured grid consisting of quadrilateral finite volumes was utilized for a spatial discretization of the problem (see Fig. 1(b)). The grid was generated by using commercial meshing software Gambit 2.4 [14]. The spherical shell was initially split into 8 equal volumes and then each volume was separately meshed using the same grid parameters. The generated grid was stretched towards the shell boundaries allowing for an accurate resolution of temperature and velocity boundary layers.

### 2.1. DNS approach

For small and moderate $Ra$ numbers all the relevant (unsteady) scales of motion can be directly resolved on the grid and the free convection Newtonian incompressible flow inside the shell is governed by non-dimensional Navier–Stokes equations:

$$\nabla \cdot \boldsymbol{u} = 0 \tag{1}$$

$$\frac{\partial \boldsymbol{u}}{\partial t} + (\boldsymbol{u} \cdot \nabla)\boldsymbol{u} = -\nabla p + \sqrt{\frac{Pr}{Ra}}\nabla^2 \boldsymbol{u} + \theta \vec{e}_y \tag{2}$$

$$\frac{\partial \theta}{\partial t} + (\boldsymbol{u} \cdot \nabla)\theta = \frac{1}{\sqrt{PrRa}}\nabla^2 \theta, \tag{3}$$

where $\boldsymbol{u} = (u, v, w)$, $p$, $t$, and $\theta$ are the dimensionless velocity, pressure, time and temperature, respectively, and $\vec{e}_y$ is the unit vector in $y$ direction. Assuming constant flow properties and applying Boussinesq approximation for temperature–velocity coupling the equations are rendered dimensionless using the scales $L = (D_o - D_i)/2$, $U = \sqrt{g\beta L \Delta T}$, $t = L/U$, and $P = \rho U^2$ for length, velocity, time and pressure, respectively. Here $L$ is the shell depth, $\rho$ is the mass density, $g$ is the gravitational acceleration, $\beta$ is the isobaric coefficient of thermal expansion, and $\Delta T = T_h - T_c$ is the temperature difference between the hot and cold boundaries. The non-dimensional temperature $\theta$ is defined as $\theta = (T - T_c)/\Delta T$. The Rayleigh and Prandtl numbers are $Ra = \frac{g\beta}{\nu\alpha}\Delta T L^3$ and $Pr = \nu/\alpha$, where $\nu$ is the kinematic viscosity, and $\alpha$ is the thermal diffusivity. The governing Eqs. (1)–(3) were solved with a buoyantBoussinesqPimpleFoam solver which is a part of an open source parallelized code openFoam developed by Weller et al [15]. The simulations were performed on a standard unix cluster and involved up to 256 cores running in parallel. PISO algorithm [16] was used for pressure-velocity coupling and conservative second order finite volume scheme was utilized for the spatial discretization. The time derivative in the momentum and the energy equations was approximated by the second order backward finite difference. No slip boundary conditions were imposed to all velocity components and a zero pressure gradient was assumed normal to the all walls when solving Poisson's equation.

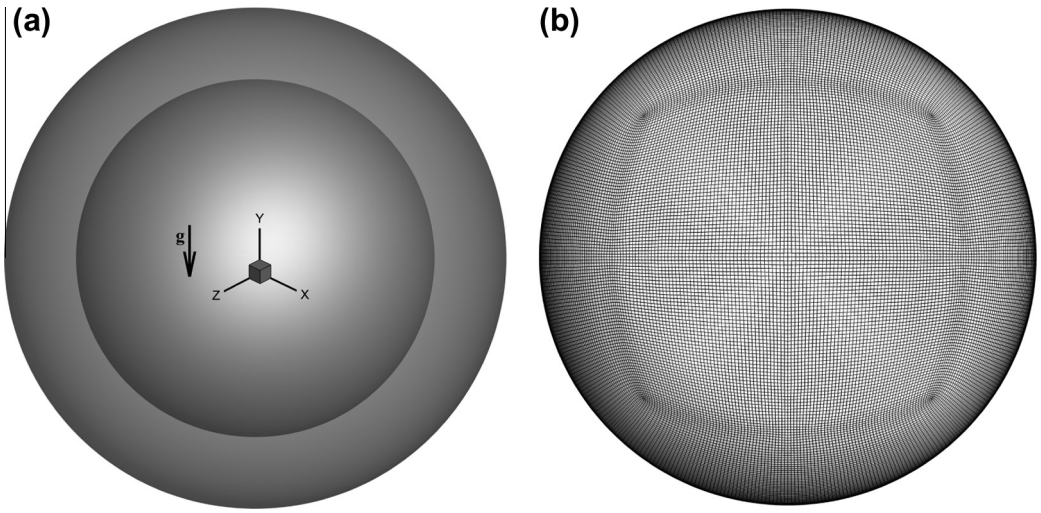


**Fig. 1.** Physical and numerical model : (a) geometry and coordinate system; (b) pseudo-structured computational grid.

Author's personal copy



### 2.2. LES approach

Large eddy simulation is typically applied for the analysis of transitional flows where the full resolution of all unsteady flow scales by DNS becomes prohibitively expensive due to extremely high computational demands. In LES the larger three-dimensional unsteady turbulent motions are directly resolved, while the modeling is applied to simulate the effects of the smaller scale motions. A dynamic one-equation eddy viscosity model which is a modification of a statically-derived subgrid scale (SGS) kinetic energy model introduced by Yoshizawa and Horiouti [17] was used to simulate fully 3-D turbulent convective flow:

$$\frac{\partial K_{sgs}}{\partial t} + (\bar{\boldsymbol{u}} \cdot \nabla) K_{sgs} - \nabla \cdot (v_{eff} \nabla K_{sgs}) = 2 v_{sgs} \overline{S}^2 - C_\epsilon K_{sgs}^{1.5} / \overline{\Delta}. \quad (4)$$

where a simple top-hat filter with a size of $\overline{\Delta}_i = (V_i)^{1/3}$ was utilized. Here $\overline{S} = 1/2(\partial \overline{U_i}/\partial x_j + \partial \overline{U_j}/\partial x_i)$ is the filtered rate-of-stress tensor. By implying the Boussinesq assumption the SGS kinematic viscosity and kinetic energy are related trough $v_{sgs} = C_k \overline{\Delta} \sqrt{\overline{K_{SGS}}}$ while the effective kinematic viscosity $v_{eff}$ is modeled as a sum of the molecular kinematic viscosity $v$ and the SGS kinematic viscosity $v_{sgs}$. $C_k$ and $C_\epsilon$ coefficients are dynamically calculated in accordance with the openFoam formalism. Eq. (4) is simultaneously solved with Navier Stokes Eqs. (1)–(3), whose diffusion terms are now account also for the modeled SGS kinematic viscosity $v_{sgs}$.

### 2.3. RANS approach

The fully developed turbulent flow was modeled by utilizing RANS approach based on $k$–$\epsilon$ model with standard wall functions [18] for modeling wall effects. An axi-symmetric flow was assumed and simulated inside a 5° span spherical segment with "wedge" boundary conditions, in accordance with the openFoam formalism. The later infers zero gradient of all flow properties normal to the segment lateral boundaries. The system of time averaged Navier–Stokes equations was simultaneously solved with two additional transport equations for kinetic energy $k$ and dissipation rate $\epsilon$. The turbulent kinematic viscosity modeled as $v_t = C_\mu k^2/\epsilon$ ($C_\mu$ is a constant equal to 0.09) contributes to the viscous term of time averaged momentum and energy equations. For more details about $k$–$\epsilon$ model implementation one should consult any CFD textbook e.g. [16].

### 2.4. Calculation of wall heat fluxes

For DNS and LES simulations no wall functions were used for the near wall effects modeling. For LES approach an accurate prediction of the wall heat fluxes was achieved by verifying the dimensionless distance from the wall $y^+ < 3$ at all nearest to wall grid cells for the entire range of $Ra$ numbers. In this case the average Nusselt number functions was calculated by:

$$Nu = \frac{1}{\pi D_o D_i} \oint \frac{\partial \theta}{\partial \hat{\eta}} dA, \quad (5)$$

where $\hat{\eta}$ is the non-dimensional normal, $D_i$ and $D_o$ are non-dimensional internal and external diameters respectively and $dA$ is non-dimensional infinitesimal area. At the same time RANS modeling with a standard wall functions for the near wall effects treatment imply the average Nusselt number to account also for the modeled turbulent viscosity:

$$Nu_t = \frac{1}{\pi D_o D_i} \oint \frac{\partial \theta}{\partial \hat{\eta}} \left(1 + \frac{v_t Pr}{v Pr_t}\right) dA, \quad (6)$$

where the constant value of turbulent Prandtl number $Pr_t = 0.9$ was chosen as the best approximation for the most of the boundary layer [19].

## 3. Verification study

DNS results were extensively verified using existing benchmark data for steady and slightly supercritical flows. Unfortunately, there is a lack of experimental and numerical data available for transitional fully 3-D natural convection flows with $Pr = 0.71$ inside narrow spherical shells. 3-D DNS analysis was performed in past for $\phi = 0.714$ and $Ra \leqslant 10^5$ values [12], while the experimental results are either related to thicker shells [20] or $Ra \leqslant 10^7$ [21]. The Nusselt number measurements for confined turbulent convection have been recently extended to up to $Ra = 10^{15}$ by conducting experiments in pressurized helium, air and nitrogen [22,23] and even up to $Ra = 10^{17}$ by using cryogenic helium gas inside a cylindrical enclosure [24,25]. However all of them are related to a Rayleigh–Bénard convection and can not be directly projected to the spherical shell geometry. Therefore the further verification of the LES results was mainly based on a presently verified DNS data. In the following we give details of the verification study conducted for both DNS and LES approaches.

### 3.1. Verification of the DNS results

An axi-symmetric, steady, laminar flow exists at small $Ra$ and is characterized by two flow patterns originally termed by [26] as crescent and kidney shape eddies. Both patterns are basically built by thin high speed layers immediately adjacent to the shell boundaries, while the bulk flow in the middle of the shell is relatively slow. The pattern existence is directly related to the shell thickness, as determined by $\phi$. The first pattern is observed for the wide range of $0.32 \leqslant \phi \leqslant 0.85$ as summarized by Powe et al. [8] while the second one only shows up in the range of $0.45 \leqslant \phi \leqslant 0.65$ and characterized by slightly higher $Ra$ numbers. In the both cases the average $Nu$ numbers predicted by fully 3-D simulations are in a good agreement with the corresponding values previously reported for axi-symmetric flow as summarized in Table 1. As the $Ra$ value increases a steady–unsteady transition takes place resulting both in a symmetry breaking (the flow becomes fully 3-D) and in emergence of different flow patterns (see [8] for more details). As a general trend, the steady-unsteady transition $Ra$ value is decreasing rapidly with increasing of $\phi$ and is proportional to $O(10^5)$ for deep ($\phi \approx 0.5$) and to $O(10^3)$ for narrow ($\phi \approx 0.9$) shells respectively. In the present study the spiral and falling vortices flows were numerically simulated for the verification purposes. The former is characterized by very slight oscillations of temperature and velocity fields (see Fig. 2-a) about their previously axi-symmetric state while the later comprises multi-cellular velocity pattern located at the upper part of the shell with temperature sparks instantly rising up and disappearing from the top side of the inner shell boundary as shown in Fig. 2-b. As a rule a realistic slightly supercritical 3-D flow demonstrates an enhanced heat flow rate through the shell for the same operating conditions compared to its axi-symmetric idealization. The $Nu$ numbers obtained for unsteady 3-D flow are considerable higher then those computed with the assumption of axi-symmetric flow (printed in brackets in Table 2). At the same time an excellent agreement exists for $Nu$

**Table 1**
Average Nu numbers for steady laminar axi-symmetric flow.

| $\phi$ | $Ra$ | Present | Ref. [27] | Ref. [28] | Ref. [29] |
|---|---|---|---|---|---|
| 0.5 | $1.0 \times 10^2$ | 1.0217 | 1.001 | 1.000 | |
| | $1.0 \times 10^3$ | 1.104 | 1.0990 | 1.1310 | 1.1021 |
| | $1.0 \times 10^4$ | 1.9665 | 1.9730 | 1.9495 | 1.9110 |
| | $1.0 \times 10^5$ | 3.4012 | 3.4890 | 3.4648 | 3.3555 |
| 0.667 | $1.0 \times 10^3$ | 1.04825 | 1.001 | 1.00115 | |
| 0.833 | $1.0 \times 10^3$ | 1.011 | 1.0 | 1.0018 | |

Author's personal copy



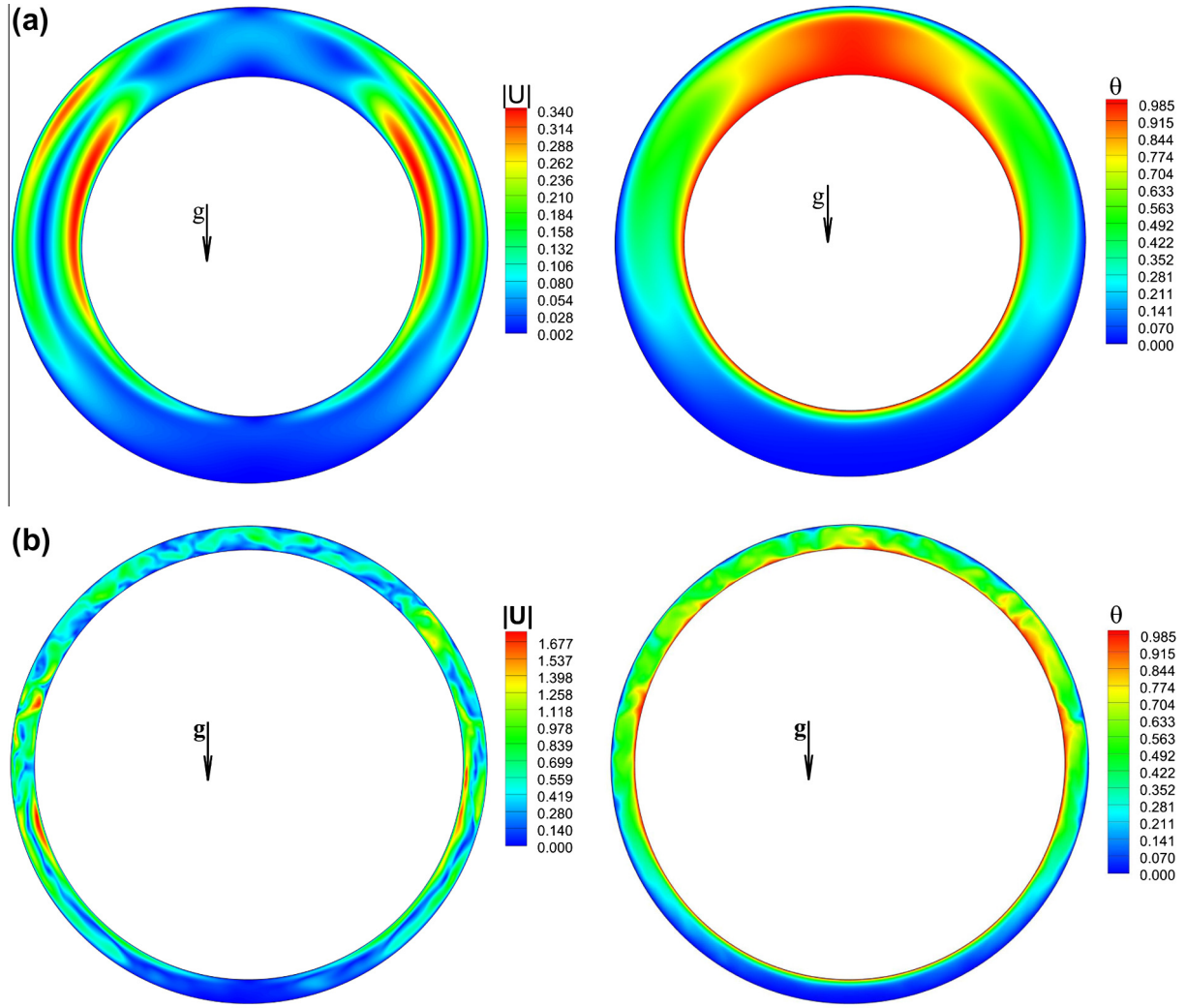


**Fig. 2.** Snapshots of velocity and temperature distribution of a slightly supercritical flow: (a) $\phi = 0.714$, $Ra = 5 \times 10^4$; (b) $\phi = 0.9$, $Ra = 10^4$.

**Table 2**
Average Nu numbers for unsteady 3-D flow.

| $\phi$ | $Ra$ | Present | Ref. [27] | Ref. [28] | Ref. [12] |
|---|---|---|---|---|---|
| 0.667 | $1.0 \times 10^4$ | 1.793 | (1.073) | (1.07138) | |
| | $1.0 \times 10^5$ | 3.243 | (1.917) | (1.89756) | |
| 0.714 | $5.0 \times 10^4$ | 2.6358 | | | 2.655 |
| | $7.0 \times 10^4$ | 2.8614 | | | 2.85 |
| 0.833 | $1.0 \times 10^4$ | 1.6523 | (1.001) | (1.0028) | |
| | $1.0 \times 10^5$ | 3.0678 | (1.008) | (1.0100) | |

when compared with the recent results of Scurtu et al. [12] who utilized the 3-D spectral code [30] for simulation of fully 3-D flow in a spherical shell with $\phi = 0.714$. In all cases the same average $Nu$ values up to the third decimal digit were obtained for the external and internal shell boundaries favorably verifying the heat flux conservation over the entire computational domain. The results of Scurtu et al. recently reported in [31] and consequently refined in [12] provide a basis for the further verification of our solutions in terms of temporal-spatial distribution of the temperature and velocity patterns. Fig. 3 shows pattern snapshots of velocity components (radial $v_r$, azimuthal $v_\theta$ $(0 \leqslant \theta \leqslant 2\pi)$ and meridional $v_\phi$ $(0 \leqslant \phi \leqslant \pi)$) and temperature on the midrange spherical surface $(D = (D_i + D_o)/2)$ of the shell for $Ra = 5 \times 10^4$. The flow is characterized by twelve separate convective cells in the form of petals evenly distributed along the shell azimuthal coordinate $\theta$. The presented pattern is rotating clockwise in azimuthal direction but theoretically could also rotate counterclockwise since no preference can exist between them. Following the formalism introduced in [12] this flow regime is described as a traveling wave and located on one of the two branches characterizing the dynamics of slightly supercritical flow.

It is remarkable that despite the periodic character of the flow the total kinetic energy and Nusselt numbers computed at $Ra = 5 \times 10^4$ for internal and external boundaries converge to constant values as shown in Fig. 4(a) and (b) respectively and was also reported by Scurtu et al [12]. The later is explained by the periodicity of the flow whose pattern is rotating as single unit and not affecting the integral values of kinetic energy and heat flux. Note also the higher oscillation amplitude of the external boundary Nusselt number $Nu_o$ compared to the corresponding values internal boundary $Nu_i$ value which is apparently a consequence of more pronounced temperature oscillations.

### 3.2. Verification of the LES results

As in any turbulence modeling process, LES should be carefully interrogated to assure the correct understanding and interpretation of the obtained results. Fig. 5 demonstrates qualitative comparison between the typical DNS and LES instanteneous

Author's personal copy



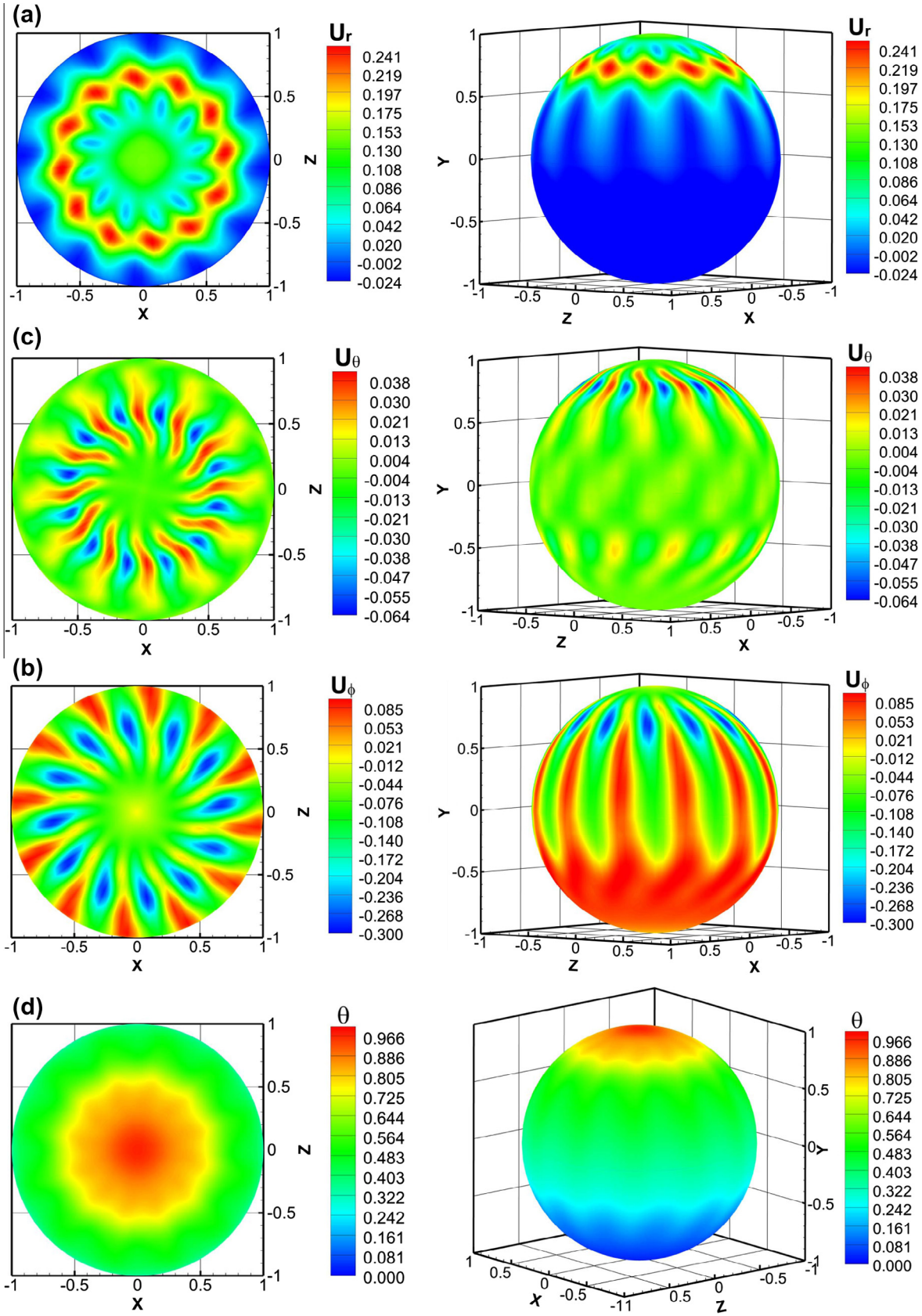


**Fig. 3.** Snapshots of the flow patterns on the midrange $D = (D_i + D_o)/2$) spherical surface, $\phi = 0.714$, $Ra = 5 \times 10^4$: (a) radial velocity $v_r$; (b) azimuthal velocity $v_\theta$; (c) meridional velocity $v_\phi$; (d) temperature $\theta$.

temperature and radial velocities on a surface midway between the two shells. Here we consider $Ra = 10^6$ for the narrow shell characterized by $\phi = 0.95$. The DNS and LES approaches yield close results for the both fields. The complex distribution of temperature and radial velocity patterns in azimuthal direction is typical for statistically stationary flow. In spite of the visually chaotic charac-

Author's personal copy



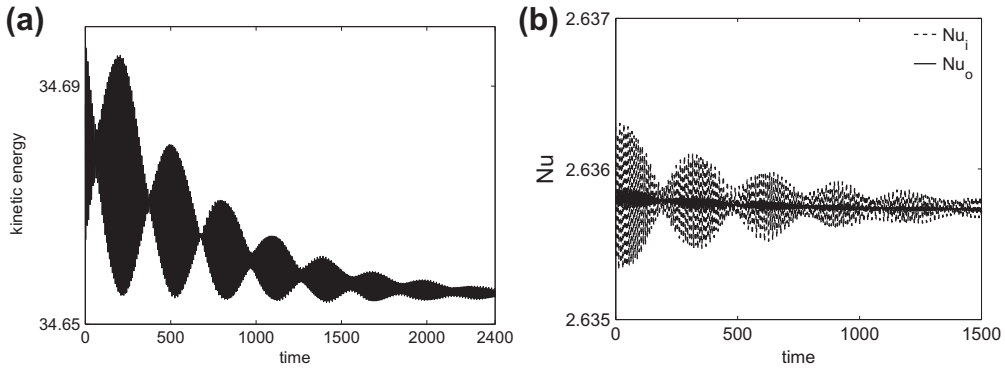


**Fig. 4.** Average values of : (a) total kinetic energy; (b)internal and external Nu number; $\phi = 0.714$, $Ra = 5 \times 10^4$.

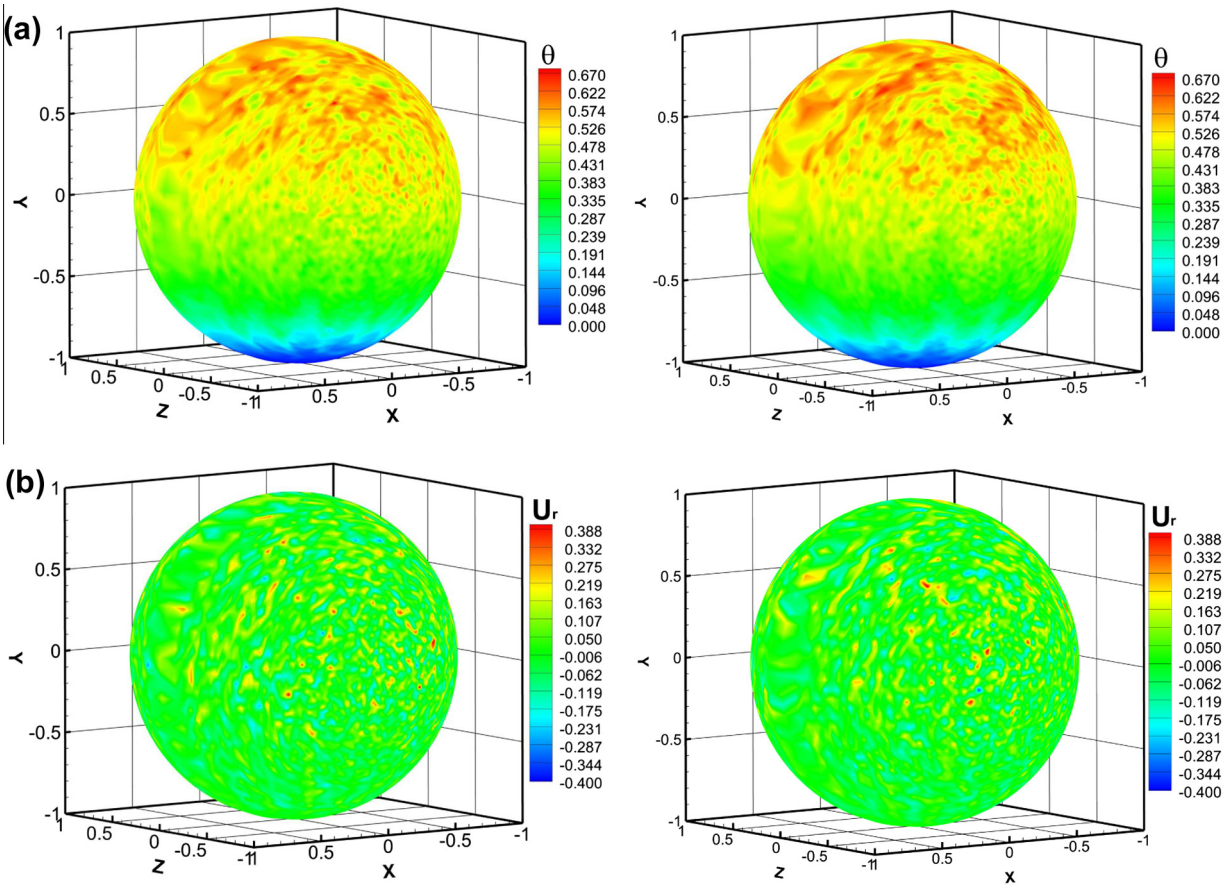


**Fig. 5.** DNS (left)-LES (right) comparison of instant : (a) temperatures $\theta$; (b) radial velocities $U_r$; obtained for $Ra = 10^6$, $\phi = 0.95$ and projected on the shell midrange surface.

ter, the general trends in the temperature and radial velocity distributions reveal a hotter region starting at the top and ending just below the equator of the shell, and a colder region located close to the shell bottom. It can also be seen that the most dynamically active zone coincides with the hotter region while the colder one is close to the thermal equilibrium and is almost static.

Obtaining grid independent results is additional critical milestone of the present verification study. This can be achieved by increasing of the grid resolution until no significant changes (up to a given numerical precision) are found between the results obtained on the two sequential grids. Unfortunately, for fully 3-D simulations this approach is often unrealistic due to extremely high computational demands and long times, necessary to collect the required statistics. Presently, we restricted the grid independence study to the two representative cases: comparison between the DNS results obtained for the $Ra = 10^6$ on the grids containing $3 \times 10^6$ and $24 \times 10^6$ volumes; comparison between the LES results for the $Ra = 10^8$ obtained on the the grids containing $4 \times 10^6$ and $32 \times 10^6$ volumes. Both tests were performed for the value of $\phi = 0.9$. For both cases we did not recognize any significant deviations between the qualitative flow characteristics. The difference between the corresponding averaged *Nu* values did not exceed 5% which is probably a little higher than that ideally expected for benchmark quality results but still too small to have any significant effect on the *Nu*–*Ra* relationship derived in the next section.

We summarize the LES verification study by presenting a power spectral density (PSD) analysis for radial velocity and temperature

Author's personal copy



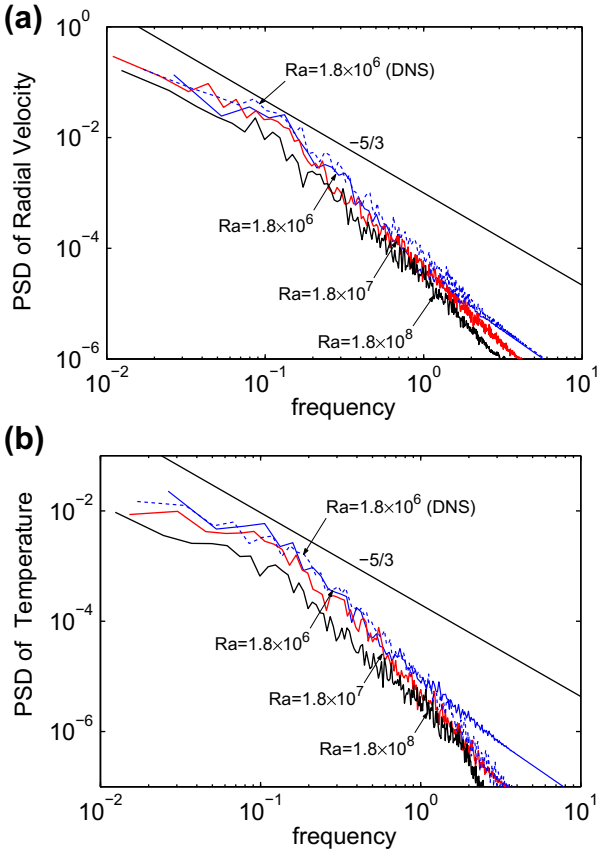


**Fig. 6.** Power spectral density monitored in the midway between the tops of internal and external boundaries, $\phi = 0.95$: (a) radial velocity; (b) temperature.

monitored by DNS at $Ra = 1.8 \times 10^6$ and by LES at $Ra = 1.8 \times 10^6$, $1.8 \times 10^7$, $1.8 \times 10^8$ as shown in Fig. 6(a) and (b). The signal was taken at the midway between the tops of the shell internal and external boundaries, in the middle of instantaneous thermal and velocity plumes, were turbulence intensities of the both quantities are small compared to the corresponding average values and the turbulent flow is statistically homogeneous. The later allows applying of Taylor's hypothesis for approximation of spatial correlations by temporal correlations (see e.g.[32]). As can be seen from the Fig. 6 a good agreement exists for the both radial velocity and temperature PSDs yielded by DNS and LES for low and mid frequencies at $Ra = 1.8 \times 10^6$. The discrepancy between the results is increasing for the high frequencies which were filtered out by a dynamic LES filter. Looking at the obtained PSD one can recognize that the range of mid frequencies closely proportional to the $f^{-5/3}$ rapidly broads with increasing of the $Ra$ number. The later illustrates the generation of fully developed turbulence in the flow bulk in agreement with the Kolmogorov spectrum observed for inertial range of the statistically homogeneous turbulent flow.

## 4. Results and discussion

### 4.1. Narrow shell analysis : DNS results

We start the discussion with the comparison between $Nu$–$Ra$ relationship computed for the laminar steady flows ($10^3 \leqslant Ra \leqslant 10^6$, and $\phi$ values, $0.5 \leqslant \phi \leqslant 0.95$) and the previously published engineering correlations. The correlation experimentally derived by Scanlan et al. [21] is among the most popular in the engineering and scientific community due to its simplicity and a wide range of applicable $\phi$, $Ra$ and $Pr$ values. In accordance with the notations adopted in the present work the Scanlan et al. [21] correlation reads:

$$Nu = 0.228(Ra^*)^{0.226}, \quad 0.7 < Pr < 4148, \quad 0.356 < \phi < 0.917. \tag{7}$$

Here $Ra^* = 2RaL/D_i$ a modified Rayleigh number introduced to scale out the effect of different shell widths. Another widely used correlation was proposed by Raithby and Hollands [33]:

$$Nu = 0.512\left(\frac{\phi^3(1-\phi)}{(1+\phi^{7/5})^5}\right)^{0.25} Ra^{0.25}, \quad Pr = 0.719. \tag{8}$$

According to the authors [33] the correlation is valid when the boundary layer is thin compared to the radius of the shell boundaries and the flow is laminar. Finally we include the correlation proposed by Teerstra et al. [34] based on linear superposition of convection and conduction solutions:

$$Nu^* = 2\sqrt{\pi}\frac{1}{1-\phi} + \left(Nu_{tr}^{-n} + Nu_{bl}^{-n}\right)^{-\frac{1}{n}}, \tag{9}$$

where $n = 2$ is suggested and $Nu_{tr} = \frac{\sqrt{2}}{11520}\left(\frac{(1-\phi)^3}{\phi^2(1+\phi)}\right)Ra^*$, $Nu_{bl} = 0.521\frac{Ra^{*0.25}}{(1+\phi^{7/5})^{5/4}}$ are the the transitional and the boundary layer Nusselt numbers respectively. In this case the modified Rayleigh number $Ra^*$ was computed by choosing the length scale as a square root of the inner sphere area ($\sqrt{\pi}D_i$). Unlike the correlation of Scanlan et al. [21] the formulas of Raithby and Hollands [33] and Teertstra et al. [34] explicitly depend on the ratio of diameters $\phi$.

Fig. 7 compares the $Nu$-$Ra$ relationship obtained by DNS for $Ra$ (or $Ra^*$) $\leqslant 10^5$ with the results predicted by correlations for $0.5 \leqslant \phi \leqslant 0.95$. While insignificant differences exist between the results predicted by engineering correlations, three general trends are evident. First, for the relatively deep shells ($0.5 \leqslant \phi \leqslant 0.714$) the correlated results are in good agreement (within 10%) with those obtained by the CFD simulations. Second, for the narrow shells ($0.85 \leqslant \phi \leqslant 0.95$) the discrepancies between the correlated and numerically predicted $Nu$ numbers increase with increasing $\phi$ value reaching up to 40% when compared with the correlation of Scanlan et al. [21] and about 30% and 20% when compared with the correlations of Raithby and Hollands [33] and Teertstra et al. [34] respectively. The third trend evident in Fig. 7 is that for the narrow shells ($0.85 \leqslant \phi \leqslant 0.95$) the $Nu$–$Ra$ (or $Nu$–$Ra^*$) relationship is characterized by much steeper slopes then those predicted by the engineering correlations. It can be also concluded (see Fig. 7-a) that the modified $Ra^*$ number introduced by Scanlan et al. [21] efficiently scales out the effect of shell width for only deep shells, while for the narrow shells ($\phi \geqslant 0.85$) a rapidly increasing scattering of the $Nu$ values is observed.

### 4.2. Narrow shell analysis : LES results

Fig. 8 summarizes LES results for $Nu$–$Ra^*$ relationship obtained for the values of $\phi = 0.85$, 0.9, 0.95 and $Ra^*$ up to $2 \times 10^8$ with the superimposed DNS results obtained for the low $Ra^*$ numbers. Note an excellent agreement between the average $Nu$ values predicted by both LES and DNS approaches for 5 different cases which verifies a correct resolving of the near wall temperature gradients by the LES model. We also verified that the same time-averaged value of Nu was obtained at both external and internal boundaries confirming the conservation of the heat flux trough the shell boundaries. It is evident that both the DNS and LES approaches collapse fairly well on a power-law relation for $Nu$–$Ra^*$ relationship but at the same time yield considerably higher slopes when compared to Scanlan et al. [21]. The higher slope infers an enhanced heat flux rate intrinsic to the narrow shells for even slightly super critical re-

Author's personal copy



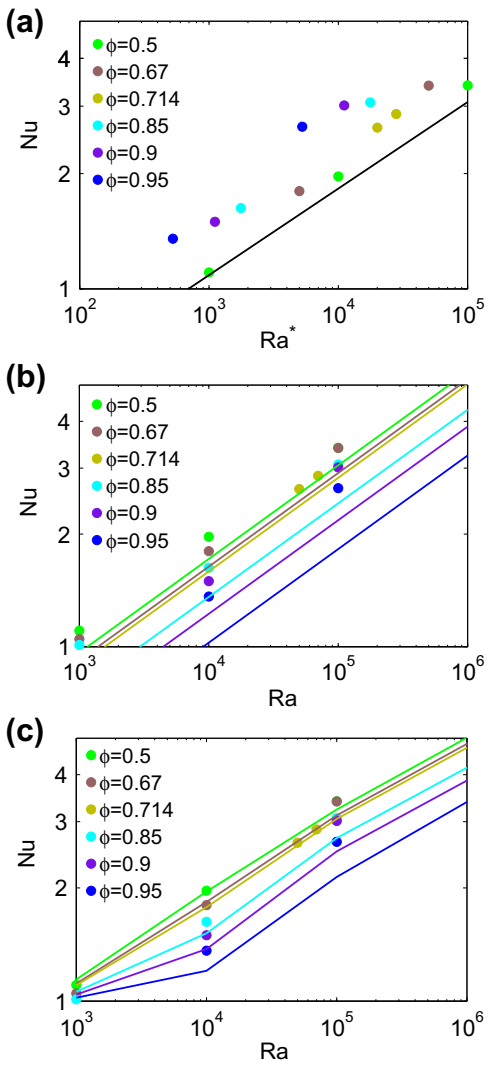


**Fig. 7.** Comparison between $Nu$–$Ra^*$ and $Nu$–$Ra$ relationship predicted by engineering correlations and numerical results for steady and slightly supercritical flows inside narrow shels: (a) Scanlan et al. [21] correlation; (b) Raithby and Hollands correlation [33]; (c) Teertstra et al. [34] correlation.

gimes. It is remarkable that about the same value of the $Nu$–$Ra$ slope ($Nu \propto Ra^{\approx 0.3}$ was also observed both numerically [35,36] and experimentally [37] for turbulent natural convection inside differentially heated cavities. The reported simulations were performed up to moderate $Ra < 10^{10}$ values of Rayleigh numbers, for which the thinnest conductive layers near the walls still exist and are not penetrated by the nearest small-scale turbulence flow structures. We would expect the same behavior for the narrow shell configuration, characterized by close to each other vertical and horizontal boundaries whose local curvature at the near equatorial and pole regions can be neglected.

As follows from the Fig. 8(a), the modified $Ra^*$ in itself does not scale out the shell width effect for the narrow shells ($0.85 \leqslant \phi \leqslant 0.95$) and three separate $Nu$–$Ra^*$ curves for each $\phi$ are observed. Noting the monotonic growth of the $Ra^*$ coefficient with $\phi$, corresponding to the curve intercept, and a very slight variation of the $Ra$ power (≈0.30 up to a second decimal digit), we suggest a new scaling which would explicitly account for gap width:

$$Nu = (0.35\phi - 0.12)Ra^{*0.3}, \quad 0.85 \leqslant \phi \leqslant 0.95, \; 10^3 \leqslant Ra^* \leqslant 2 \times 10^8. \tag{10}$$

The scaled results collapse on a single curve as shown in Fig. 8(b). It should be noted that the suggested correlation was derived and numerically verified for $Pr = 0.71$ and only the range $Ra^*$ and $\phi$ values given in Eq. (8). We would not recommend to apply it for extended range of $\phi$ and $Pr$ values without additional validation (numerical or experimental). At the same time the developed methodology and general observations regrading the free convection flow features intrinsic to narrow shells at a given range of $Ra$ values are believed to be general and may be useful for the future research in this area.

### 4.3. Narrow shell analysis : RANS results

We now turn to the RANS results. RANS modeling of the fully turbulent confined flow is challenging because the very thin boundary layers cannot be resolved on the coarse grid, and so-called *wall functions* must be used. In this case a simple grid refinement does not yield a grid independent results since the standard wall functions are only valid when the first grid point is within the logarithmic region, i.e. when $30 < y^+$. As a result such wall functions are only appropriate in the higher Ra number regime; when RANS is used at lower values of $Ra$, the wall model must be modified or switched off entirely. We found that the later can introduce significant uncertainties and thus we restrict the RANS results here to $10^8 \leqslant Ra \leqslant 10^{12}$, where the flow can safely be assumed fully turbulent, statistically stationary, axi-symmetric and we can verify the correct wall-model implementation.

Fig. 9 demonstrates RANS results obtained for $Ra = 10^{12}$ and $\phi = 0.85$, 0.9, and 0.95 in terms of normalized velocity magnitude (left) and temperature (right) fields. One can recognize a qualitative difference in the averaged velocity magnitude distribution be-

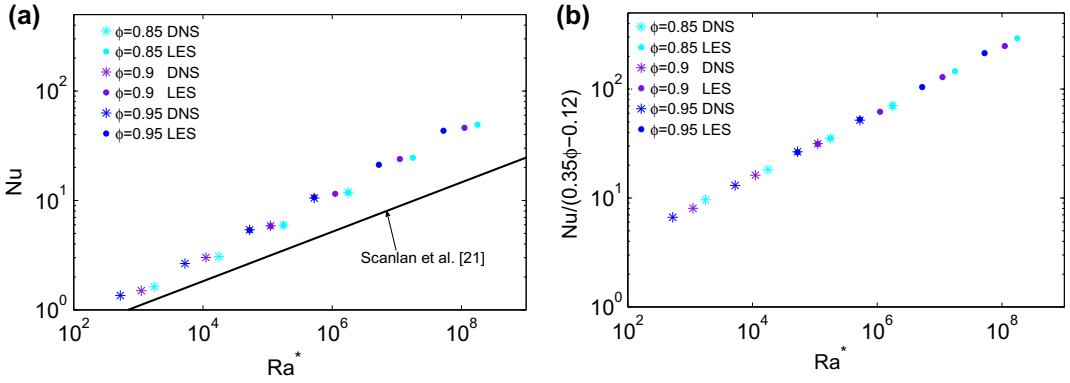


**Fig. 8.** DNS and LES results for the $Nu$–$Ra^*$ relationship: (a) three separate sets for $\phi = 0.85$, 0.9, 0.95; (b) a uniform curve.

Author's personal copy



tween the deepest shell ($\phi = 0.85$) and the two narrower shells ($\phi = 0.9, 0.95$). The former (see Fig. 9(a)) is still characterized by a single convection cell occupying almost the whole shell volume. Looking at the narrower shell ($\phi = 0.9$, Fig. 9(b)) two convection cells can be recognized: the smaller one is adjacent to the shell north pole, while the larger occupies almost the rest of available volume. Finally the narrowest shell ($\phi = 0.95$) is characterized by 3 convection cells, two of which are almost of the same size, located at the shell top and occupy approximately 1/5 of the shell's volume, while the rest of it is occupied by the third cell. Note also the steep decrease in maximal normalized velocity values when comparing shells characterized by $\phi = 0.85$ and $\phi = 0.9$ which is apparently related to the change from a single to double cell spatial topology. In contrast, further increasing of $\phi$ to 0.95 results in a higher maximal value of the averaged velocity magnitude (see Fig. 9(c)). There is a narrow high velocity region close to the north pole of the shell (see Fig. 9(a)) for $\phi = 0.85$ and $\phi = 0.9$ values (see Fig. 9(a) and (b)) that does not occur in the narrowest shell(see Fig. 9(c)). The observation suggests an enhanced mixing that increases with the $\phi$.

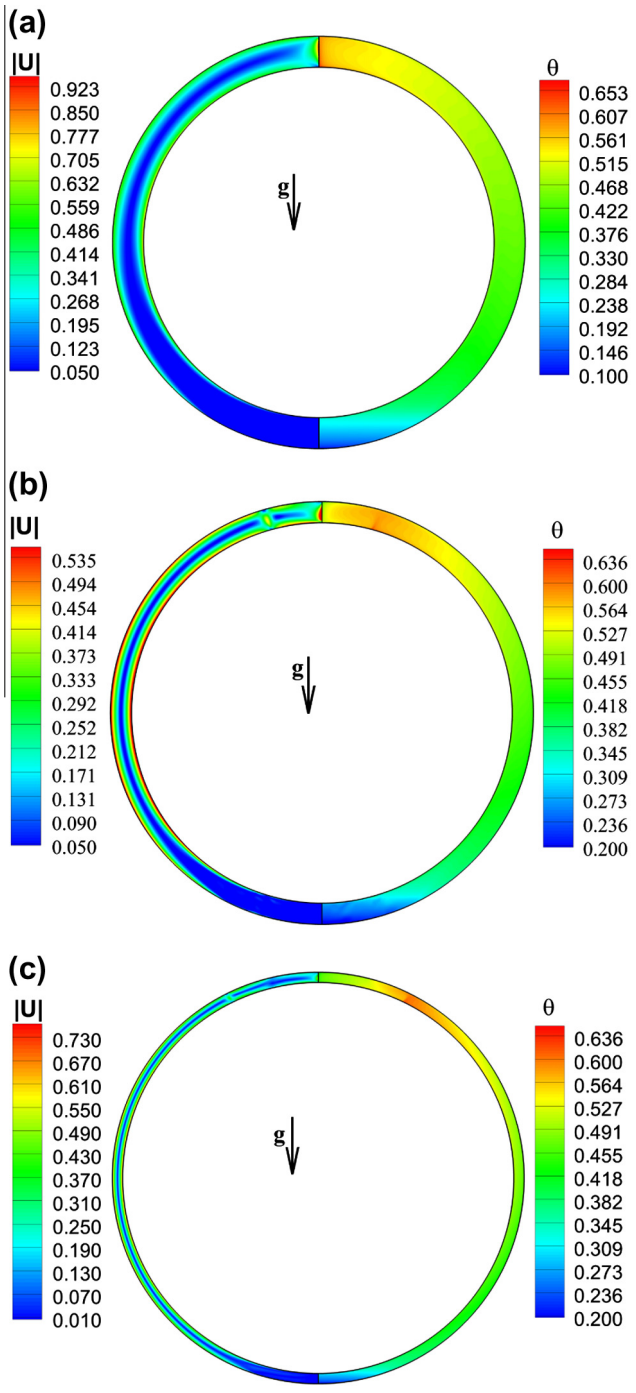


**Fig. 9.** Normalized velocity magnitude (left) and temperature (right) fields obtained by RANS simulation, $Ra = 10^{12}$: (a) $\phi = 0.85$; (b) $\phi = 0.9$; (c) $\phi = 0.95$.

The averaged spatial distribution of temperature shares the same general characteristics with those of the averaged velocity magnitude field. A single, double and triple convection cell pattern developed in the deepest($\phi = 0.85$), narrower ($\phi = 0.9$) and the narrowest ($\phi = 0.95$) shells respectively can be easily recognized. On the other hand there is no large difference between the maximal temperature values of different shell widths. This is because the fully developed turbulent temperature field provide the similar thermal mixing independently on the shell width. Note also the very thin boundary layers inherent to the both velocity and temperature fields which tend to decrease with the shell width.

The RANS analysis is summarized by plotting the results for the suggested $Nu$–$Ra^*$ relationship superimposed with previously obtained DNS and LES results as shown in Fig. 10. It appears that in contrast to DNS and LES results the dependence of the turbulent results on $\phi$ is not very well scaled by proposed $Nu$ scaling. In addition the slope of the best fit curve, obtained for the turbulent results is much higher $\propto Ra^{0.4}$ then that previously found for the DNS and LES results $\propto Ra^{0.3}$. The results are suggestive of a different turbulent flow regime, characterized by even more enhanced heat transfer flux rate. It is remarkable that the transition between the two regimes takes place at about $Ra^* = 10^9$ (or $Ra = 10^{10}$) which is in good agreement with the work of [38] who reported the same behavior for the Rayleigh–Bénard convection inside a cylinder above approximately $Ra = 3 \times 10^{11}$. The higher, $\propto Ra^{0.4}$ is also consistent with the theoretical study of Kraichan [39] who predicted $Nu \propto Ra^{0.5}$ in the absence of any boundary layer and $Nu \propto Pr^{-0.25} Ra^{0.5}/(\ln Ra)^{1.5}$ in the presence of viscous sub-layer. Note that Kraichan's later relation is well approximated by $Nu \propto Ra^{0.42}$ for $10^8 \leqslant Ra \leqslant 10^{12}$ and $Pr = 0.71$. At the same time a number of recent works [24,25,22] did not confirm the existence of a critical $Ra$ number at which a sharp increase of the $Nu$–$Ra$ curve slope takes place. According to these investigators there is a constant $Nu \propto Ra^{0.3}$ power law relation for the entire range of $Ra$ numbers up to $Ra = 10^{16}$.

Basing on the recent work of Niemela and Sreenivasan [25] we postulate that the results suggest two independent flow regimes, characterized by either shear- or plume-dominated conditions. To understand the differences between these regimes we appeal

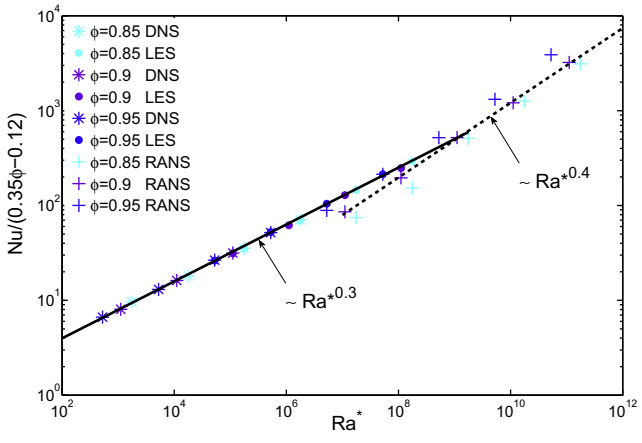


**Fig. 10.** DNS, LES, and RANS results for the $Nu$–$Ra^*$ relationship, $\phi = 0.85, 0.9, 0.95$.

Author's personal copy



to boundary layer theory, which allows us to estimate the thickness of thermal and shear boundary layers for different flows. Presently, we adopted the result of [25] who correlated the velocity/temperature boundary layer thicknesses for the Rayleigh–Bénard convection inside a cylinder as:

$$\delta/\lambda = 648\ \Gamma^{0.091} NuPr^{0.636}/Ra^{0.445}, \tag{11}$$

where $\Gamma$ is the aspect ratio defined as the ratio of the horizontal dimension of the cylinder to its vertical dimension. Note that a unity value of $\delta/\lambda$ would not necessarily distinguish between the shear- and the thermally-dominated conditions near the wall. This is because viscous-dominated effects occur only in a certain fraction of shear boundary layer thickness. At the same time if the thermal boundary layer is entirely embedded inside the viscous sublayer it is unlikely to see a high impact of the velocity boundary layer turbulence on the overall heat transport.

We might roughly say that the free convection flow inside a narrow spherical shell resembles cylindrical Rayleigh–Bénard convection only close to north pole. To quantify this statement we calculated the $\delta/\lambda$ ratio for both LES and RANS results with different aspect ratios, $\Gamma \geqslant 5$, to address narrow shell configurations. It is remarkable that while the LES results demonstrate a rapid decrease of $\delta/\lambda$ value versus $Ra$ with the minimum equal to $\delta/\lambda \approx 2.8$ for $Ra = 10^8$ (slightly varying versus $\Gamma$), the RANS results showed an asymptotic behavior of $\delta/\lambda \approx 2.3$ starting from $Ra = 10^{10}$, independently from the $\Gamma$ value. Note that the real near-wall dynamics of the flow can only be inferred, since the near wall effects in the RANS simulations were modeled by standard wall functions and not directly resolved on grid. Our interpretation is that in the first case (LES simulations, moderate $Ra$ values) the temperature boundary layer was still captured inside the velocity viscous sublayer (although the thicknesses of the both might be almost the same for $Ra = 10^8$), corresponding to shear-dominated condition. On the other hand, in the second case (RANS simulations, high $Ra$ values) an asymptotic thermally-dominated regime, at which the small-scale turbulence penetrated the thinnest conductive layer, might be reproduced. The range of $10^7 \leqslant Ra^* \leqslant 10^8$ values falls in the boundary between the two states. Then it is not surprising that there is a deviation between the overlapping LES and $k$–$\epsilon$ model results. The later predicts lower $Nu$ values, that can be a consequence of not fully developed turbulent boundary layer leading to underestimation of the turbulent wall heat flux values.

## 5. Conclusions

Laminar and turbulent free convection flow inside narrow spherical shells with isothermal cold and hot boundaries characterized by $0.5 \leqslant \phi \leqslant 0.95$ , $Pr = 0.71$ was studied. Laminar flow was carried out by DNS while transitional and turbulent flow was analyzed by applying LES and RANS approaches. The accuracy of the results was extensively verified. It was found that the steady

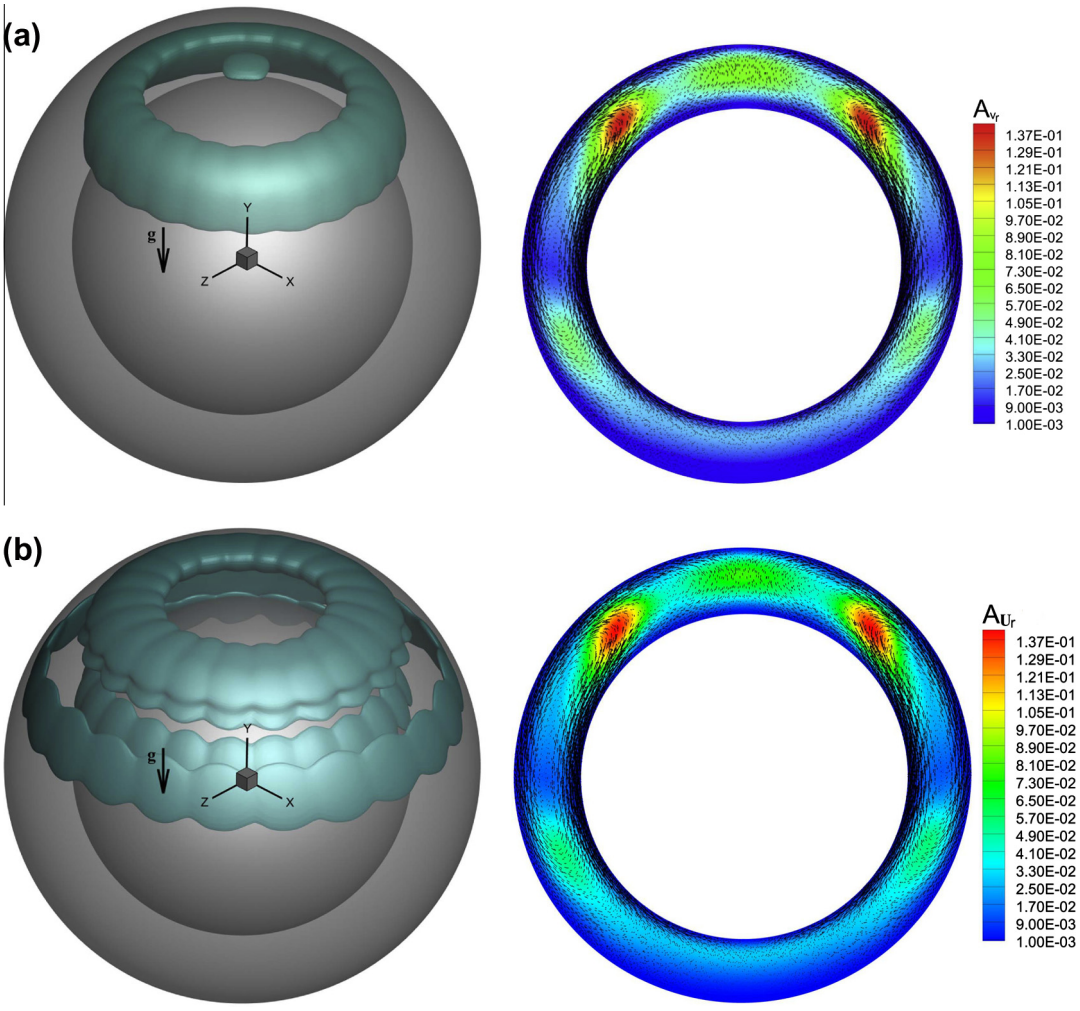


**Fig. A.11.** Iso-surfaces of the oscillation amplitudes accompanied by the corresponding mid cross section of the shell with superimposed projection of the mean velocity vector field :(a) radial velocity $v_r$; (b) azimuthal velocity $v_\theta$; (c) meridional velocity $v_\phi$; (d) temperature $\theta$.

Author's personal copy



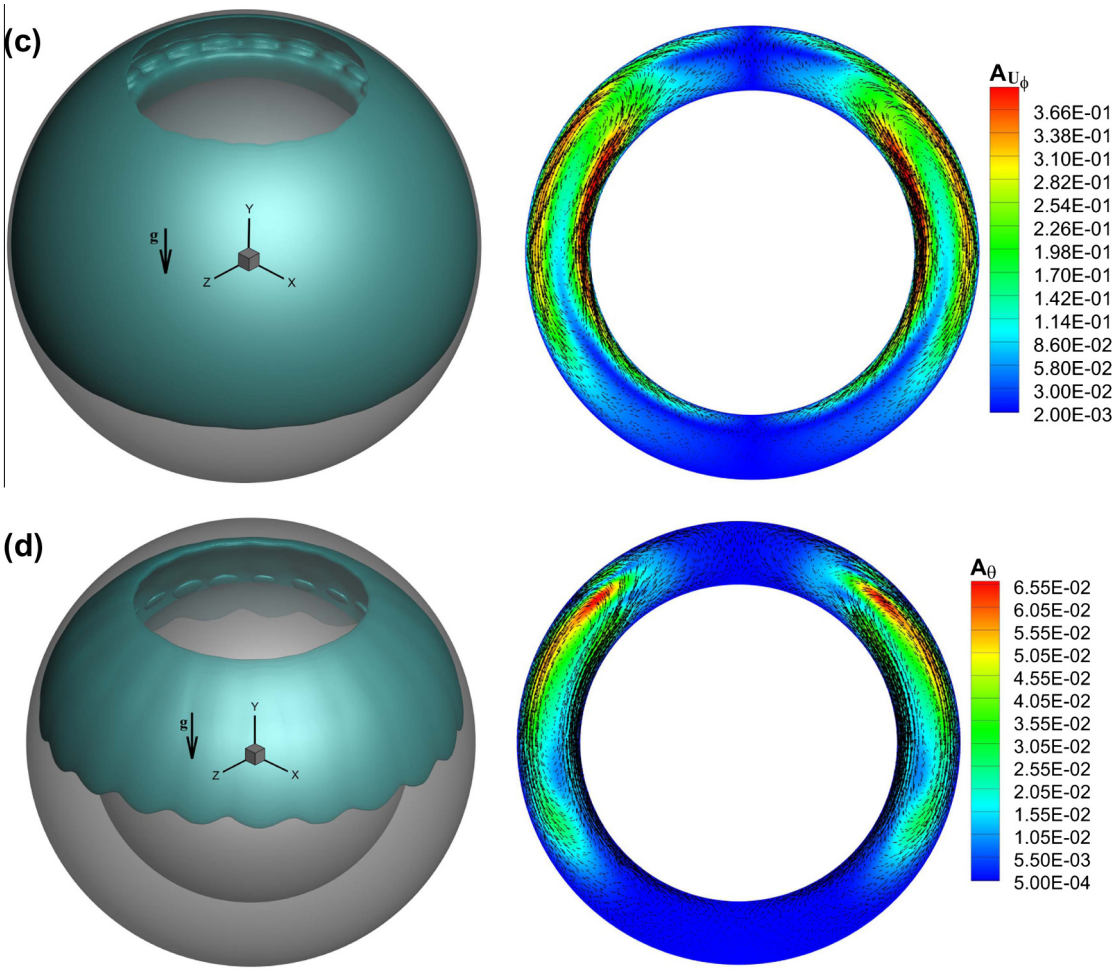


**Fig. 11.** (*continued*)

state flow pattern is axi-symmetric and characterized by a single convection cell. The cell, whose cross section is sometimes called a "crescent eddy" occupies the shell medium expanding alongside the equator and rapidly narrowing towards the shell poles. In contrast, the unsteady flow is fully 3-D with pattern strongly dependent on the shell's depth. Inside the narrow shells ($\phi \geqslant 0.85$) the flow is aperiodic and characterized by unsteady patterns known also as a "falling vortices" [40] evolving and cyclically dissolving from the shell top towards to its equator. For a deeper shell ($\phi = 0.714$) periodical temperature and velocity distributions in the form of traveling waves were observed. Turbulent flow (analyzed both by LES and RANS approaches) is in general characterized by spatially averaged temperature and velocity distributions in the flow bulk and very thin boundary layers. We also considered slightly supercritical flow with $\phi = 0.714$ in detail (see Appendix A) to provide benchmark data for future linear stability studies.

The functional dependence of average $Nu$ on $Ra$ and modified $Ra^*$ has been extensively investigated for the range of $10^3 \leqslant Ra^* \leqslant 10^{12}$ covering laminar, transitional and fully turbulent flow regimes. It was found that the deep and narrow shells feature different flow characteristics even at low $Ra$ values. In particular for the deep shells ($0.5 \leqslant \phi \leqslant 0.714$) we obtained $Nu \sim Ra^{*0.22}$ up to the $Ra^* \leqslant 10^5$ in agreement with the classical experimental work of Scanlan et al [21] and more recent numerical study of Raithby and Hollands [33] and Teerstra et al. [20]. In contrast, for the narrow shells ($0.85 \leqslant \phi \leqslant 0.95$) both slightly supercritical and transitional flows yield $Nu \sim Ra^{*0.3}$ up to $Ra^* \leqslant 2 \times 10^8$ which suggests an enhanced heat flux rate through the shell boundaries. The above result is in good agreement with the $Nu$–$Ra$ relation for Rayleigh–Bénard turbulent convection in a cylindrical container ($Nu \sim Ra^{1/3}$)[25] and in a plane layer ($Nu \sim Ra^{0.3}$)[41] as well as for natural convection inside differentially heated square [35] and tall [36] cavities, both characterized by $Nu \sim Ra^{0.33}$. A new scaling relation for $Nu$ was suggested for narrow shells $Nu$–$Ra^*$. Finally the fully turbulent convective flow in the narrow shells was simulated by RANS approach for $Ra$ up to $10^{12}$. A new flow regime characterized by an even more enhanced heat flux was revealed yielding $Nu \sim Ra^{*0.4}$ functional relation. The phenomenon may be related to transition from laminar to turbulent thermally-driven boundary layer taking place at very high $Ra$ numbers.

## Acknowledgments

This research was funded by the Jet Propulsion Laboratory (JPL), California Institute of Technology, under a contract with the National Aeronautics and Space Administration. We are grateful to the JPL for a granted access to their supercomputer facilities. We are also thankful to Dr. Jeffrey Hall for his helpful inputs during this project.

## Appendix A. Intermediate shell analysis : DNS results

To gain a more insight into dynamics of the slightly supercritical periodic flow we look at the spatial distribution of the oscilla-

Author's personal copy



tion amplitudes of each velocity component and temperature fields corresponding to the most energetic mode as shown in Fig. A.11. The amplitudes correspond to the maximum absolute deviations from the base flow averaged over several oscillation periods. The iso surfaces confine the areas at which amplitude values are not less than 50% of the maximal amplitude of the corresponding flow field. As expected the iso surfaces are periodic and occupy the upper and equatorial part of the shell where the flow is unstable and velocities attain their maximum. At the same time at the bottom part of the shell, characterized by almost stationary flow, the flow oscillations are kept to a minimum.

Each oscillation amplitude iso surface is accompanied by the corresponding mid cross section of the shell with superimposed projection of the mean velocity vector field. The section plane is crossing over the two opposite crests of each iso surface. The vectors shown in the figure are scaled by the magnitude of corresponding velocity values. Radial velocity oscillations $A_{v_r}$ (see Fig. A.11(a)) attain their maximum values close to the leading edge of each convective cell in the midway between internal and external boundaries. Taking into account that the radial and the gravity force directions are almost parallel close to the shell top, the region falls on the fringe of the thermal plume. The later is rising up from the north pole of the internal sphere which is the most unstable flow region. As a consequence the amplitude of the the azimuthal velocity associated with the wave traveling in the azimuthal direction $A_{v_\theta}$ also riches its maximum there, as shown in Fig. A.11(b). In contrast, azimuthal velocity $v_\phi$ primarily oscillates at both sides of the shell equator close to shell boundaries where the maximal $v_\phi$ velocities are observed. The phenomenon can be explained by an interaction between almost static bulk flow in the mid part of the shell and two regions of a high velocity confining it from the sides and forming an oscillating convection cell (see Fig. A.11(c)). Looking at the spatial distribution of the temperature amplitudes (Fig. A.11(d)) one can recognize that their maximal values are located closer to the external boundary at the interface between the cold stream going down along the external boundary and the hot stream originating at the internal boundary and going up along the leading edge of convective cell. Mixing of the both cold and cold streams results in large temperature oscillations localized in this region.

## References


[1] R. Clever, F. Busse, Transition to time-dependent convection, J. Fluid Mech. 65 (1974) 625–645.
[2] F. Busse, Nonlinear properties of thermal convection, Rep. Prog. Phys. 47 (1974) 1930–1967.
[3] J. Gollub, S. Benson, Many routes to turbulent convection, J. Fluid Mech. 100 (1980) 449–470.
[4] J. Curry, J. Herring, J. Loncaric, S.A. Orszag, Order and disorder in two- and three-dimensional Benard convection, J. Fluid Mech. 147 (1984) 1–38.
[5] P. Daniels, C. Ong, Nonlinear convection in a rigid channel uniformly heated from below, J. Fluid Mech. 215 (1990) 503–523.
[6] J. Gabor, L. Baker, J. Cassulo, G. Mansoori, Heat transfer from heat generating boiling pools, Chem. Eng. Prog. Ser. 73 (1977) 78–85.
[7] D. Thevenard, A. Rouzand, J. Comera, J. Favier, Influence of convective thermal oscillations on a solidification interface in bridgman growth, J. Cryst. Growth 108 (1981) 572–582.
[8] R. Powe, R. Warrington, J. Scanlan, Natural convective flow between a body and its spherical enclosure, Int. J. Heat Mass Transfer 23 (1980) 1337–1350.
[9] B. Futterer, A. Brucks, R. Hollerbach, C. Egbers, Thermal blob convection in spherical shells, Int. J. Heat Mass Transfer 50 (2007) 4079–4088.
[10] Y. Feldman, T. Colonius, M. Pauken, J. Hall, J. Jones, Simulation and cryogenic experiments of natural convection for the Titan Montgolfiere, AIAA J. 50 (2012) 2483–2491.
[11] G. Dorrington, Planetary flight surge faces budget realities, Adv. Space Res. 47 (2011) 1–19.
[12] N. Scurtu, B. Futterer, C. Egbers, Pulsating and traveling wave modes of natural convection in spherical shells, Phys. Fluids 22 (2010) 114108.
[13] Y. Feldman, A.Y. Gelfgat, Oscillatory instability of a three-dimensional lid-driven flow in a cube, Phys. Fluids 22 (2010) 093602.
[14] Gambit 2.4 Users Guide, Fluent Inc (US), 2007, <http://aerojet.engr.ucdavis.edu/gambithelp/>.
[15] H. Weller, G. Tabor, H. Jasak, C. Fureby, A tensorial approach to computational continuum mechanics using object-oriented techniques, Comput. Phys. 12 (1998) 620–631.
[16] J. Ferzirger, M. Peric, Computational Methods for Fluid Dynamics, Springer, 2002.
[17] A. Yoshizava, K. Horiuti, A statistically-derived subgrid-scale kinetic energy model for the large-eddy simulation of turbulent flows, J. Phys. Soc. Jpn. 54 (1985) 2834–2839.
[18] B. Launder, D. Spalding, Lectures in Mathematical Models of Turbulence, Academic Press, London, 1972.
[19] W. Kays, D. Crawford, Convective Heat and Mass Transfer, McGraw-Hill Book Company, 1980.
[20] P. Teertstra, M. Yovanovich, J.R. Culham, Natural convection measurements for a concentric spherical enclosure, J. Heat Transfer 128 (2006) 580–587.
[21] J. Scanlan, E. Bishop, R. Powe, Natural convection heat transfer between concentric spheres, Int. J. Heat Mass Transfer 13 (1970) 1857–1872.
[22] G. Ahlers, D. Funfschilling, E. Bodenschatz, R.J. Donnellyy, Transitions in heat transport by turbulent convection at rayleigh numbers up to $10^{15}$, New J. Phys. 11 (2009) 1–18.
[23] D. Funfschilling, E. Bodenschatz, G. Ahlers, Search for the 'ultimate state' in turbulent Rayleigh–Bénard convection, Phys. Rev. Lett (2009) 024503.
[24] J. Niemela, L. Skrbek, K. Sreenlvasan, R.J. Donnellyy, Turbulent convection at very high rayleigh numbers, Nature 404 (2000) 837–840.
[25] J. Niemela, K. Sreenivasan, Confined turbulent convection, J. Fluid Mech. 481 (2003) 355–384.
[26] E. Bishop, L. Mack, J. Scanlan, Heat transfer by natural convection between concentric spheres, Int. J. Heat Mass Transfer 9 (1966) 649–652.
[27] H. Chu, T. Lee, Transient natural convection heat transfer between concentric spheres, Int. J. Heat Mass Transfer 36 (1993) 3159–3170.
[28] A. Dehghan, K. Masih, Numerical simulation of buoyancy-induced turbulent flow between two concentric isothermal spheres, Heat Transfer Eng. 31 (2010) 33–44.
[29] C. Chiu, W. Chen, Transient natural convection heat transfer between concentric and vertically eccentric spheres, Int. J. Heat Mass Transfer 39 (1996) 1439–1452.
[30] R. Hollerbach, A spectral solution of the magneto-convection equations in spherical geometry, Int. J. Numer. Methods Fluids 32 (2000) 773–797.
[31] N. Scurtu, B. Futterer, C. Egbers, Three-dimensional natural convection in spherical annuli, J. Phys.: Conf. Ser. 137 (012017) (2008) 1–9.
[32] S. Pope, Turbulent Flows, Cambridge University Press, New York, 2000.
[33] G. Raithby, K. Hollands, A general method of obtaining approximate solutions to laminar and turbulent free convection problems, Adv. Heat Transfer 11 (1975) 265–315.
[34] P. Teertstra, M. Yovanovich, J. Culham, Analytical modeling of natural convection in concentric spherical enclosures, J. Thermophys. Heat Transfer 20 (2006) 297–304.
[35] N. Markatos, K. Pericleous, Laminar and turbulent natural convection in an enclosed cavity, Int. J. Heat Mass Transfer 27 (1984) 755–772.
[36] J. Xaman, G. Alvarez, L. Lira, C. Estrada, Numerical study of heat transfer by laminar and turbulent natural convection in tall cavities of facade elements, Energ. Build. 37 (2005) 787–794.
[37] W.H. Leong, K.G.T. Hollands, A.P. Brunger, Experimental nusselt numbers for a cubical-cavity benchmark problem in natural convection, Int. J. Heat Mass Transfer 42 (1999) 1979–1989.
[38] X. Chavanne, F. Chilla, B. Chabaud, B. Castaing, B. Hebral, Turbulent Rayleigh–Bénard convection in gaseous and liquid he, Phys. Fluids 13 (2001) 1300–1320.
[39] R.H. Kraichnan, Turbulent thermal convection at arbitrary Prandtl number, Phys. Fluids 5 (1962) 1374–1389.
[40] C. Thamire, N. Wright, Multiple and unsteady solutions for buoyancy driven flows in spherical annuli, Int. J. Heat Mass Transfer 41 (1988) 4121–4138.
[41] A. Tilgner, Convection in an ideal gas at high rayleigh numbers, Phys. Rev. E 84 (2011) 026323.